


Cite this: *Nanoscale*, 2025, **17**, 18092

Received 2nd May 2025,
Accepted 19th July 2025

DOI: 10.1039/d5nr01805f

rsc.li/nanoscale

Silver nanostructure-loaded starch functionalized magnetite (Ag/s-Fe₃O₄) photocatalyst for H₂O₂ production: experimental and molecular dynamics studies†

Uttam Kumar,^a Jyoti Kuntail,^b Shaili Pal,^c Mrinal R. Pai,^{d,e} Xenophon Krokidis,^f Andreas Bick^f and Indrajit Sinha^{id} *^a

The present research investigates photocatalytic H₂O₂ formation on a composite of Ag and starch-stabilized Fe₃O₄ (denoted as s-Fe₃O₄) nanoparticles. Starch functionalization of the Fe₃O₄ part significantly improved the hydrophilicity of the composite. The charge carrier separation efficiency and photocatalytic activity changed with the amount of Ag loading on s-Fe₃O₄. H₂O₂ production on this photocatalyst was investigated in pure water and aqueous solutions of various green sacrificial agents like glycerol. Classical molecular dynamics (MD) was employed to study the adsorption affinity of O₂ and H₂O on the surface of Fe₃O₄, s-Fe₃O₄, and Ag/s-Fe₃O₄ in an aqueous medium. MD results indicate that functionalizing Fe₃O₄ with starch (s-Fe₃O₄ system) enhances water adsorption affinity, and precipitating Ag nanostructures on s-Fe₃O₄ (Ag/s-Fe₃O₄) increases O₂ adsorption affinity. Water contact angle measurements on Fe₃O₄, s-Fe₃O₄, and Ag/s-Fe₃O₄ nanoparticles also quantify significantly better water adsorption due to starch functionalization. An aqueous solution of glycerol exhibited the best photocatalytic H₂O₂ production activity. This result is critical given that glycerol is green, economical, and a byproduct of the biodiesel industry. A photocatalysis mechanism for H₂O₂ generation on Ag/s-Fe₃O₄ photocatalysts has been proposed based on a series of control experiments and molecular dynamics simulations.

1. Introduction

Hydrogen peroxide (H₂O₂), an essential green chemical, is utilized extensively in wastewater treatment (Fenton and photo-Fenton processes), organic synthesis, disinfection, pulp bleaching, and many other applications.^{1–3} H₂O₂ has also drawn interest as a potential substitute for H₂ as a fuel cell energy carrier in single-compartment cells for electricity production.⁴ Such applications of H₂O₂ have attracted the attention of different research groups to its production process.⁵ Currently, the anthraquinone method is used for H₂O₂ production at the industrial level. The method requires significant energy consumption due to multistep hydrogenation and oxidation reactions, along with the formation of several toxic by-products.^{6,7}

Contrary to this, H₂O₂ generation by photocatalysis is a low-cost and environmentally friendly process. It uses abundant and renewable resources like water, oxygen, and sunlight.^{4,8} Photocatalytic H₂O₂ production can occur either by a two-electron O₂ reduction pathway (O₂ + 2H⁺ + 2e[−] → H₂O₂) or a series of single-electron O₂ reductions (O₂ + e[−] → [•]O₂[−] followed by [•]O₂[−] + 2H⁺ + e[−] → H₂O₂).^{9,10} Most photocatalysts reported in literature generate H₂O₂ from aqueous solutions of sacrificial agents, including methanol, ethanol, isopropanol, and oxalic acid.^{11,12} Only a few photocatalysts have reported H₂O₂ production from pure water.^{13,14} In this context, green and economical sacrificial agents can also be used. Glycerol is a byproduct of biodiesel production, green and economical, but very few publications have investigated its efficacy as a sacrificial agent.¹⁵

A significant challenge for industrial applications of heterogeneous photocatalysts is their separation from the reaction system, recycling, and reuse. Superparamagnetic photocatalysts can be separated by magnetic decantation. After separation, the external magnetic field is removed, and photocatalyst nanoparticles can be re-dispersed in a separate solution by simply stirring.^{16,17} In this context, fine Fe₃O₄ nanoparticles are superparamagnetic, economical, and have visible

^aDepartment of Chemistry, Indian Institute of Technology (Banaras Hindu University), Varanasi 221005, India. E-mail: isinha.apc@iitbhu.ac.in

^bDepartment of Chemistry, Indian Institute of Technology, Kanpur, India

^cDepartment of Chemistry, Harcourt Butler Technical University, Kanpur 208002, India

^dChemistry Division, Bhabha Atomic Research Centre, Mumbai 400085, India

^eHomi Bhabha National Institute, Anushaktinagar, Mumbai 400094, India

^fSCIENOMICS SAS, 16, rue de l'Arcade, 75008 Paris, France

† Electronic supplementary information (ESI) available. See DOI: <https://doi.org/10.1039/d5nr01805f>


range band gaps.¹⁸ Nevertheless, bare Fe₃O₄ nanoparticles suffer from poor water dispersibility. Fine Fe₃O₄ nanoparticles, stabilized by various organic modifiers such as citrate and dextrin, exhibit energy band gaps exceeding 2.1 eV due to quantum size effects and enhanced water dispersibility.^{19,20} Similarly, starch-stabilized magnetite nanoparticles display a comparable band gap and demonstrate excellent water dispersibility. Starch emerges as one of the potential functionalization agents in magnetite synthesis because it is green, abundant, and cost-effective. Starch contains many O–H functional groups, which can interact with and bind to the surface of nanoparticles during the initial nucleation stage.^{19,21}

Adding a suitable noble metal cocatalyst (like Au, Ag, Pd, and Pt) to the primary semiconductor photocatalyst has been recommended to improve charge separation, O₂ adsorption, and its reduction.^{22–24} For instance, H₂O₂ formation increases when co-catalysts like Ag or Au nanostructures are attached to the semiconductor part.^{25,26} Moreover, the nanoparticles of these noble metals efficiently absorb visible light of specific wavelengths owing to their localized surface plasmon resonance (LSPR) effect.^{27,28} The re-emission of the absorbed energy in the visible range enhances the light absorption efficiency of the photocatalyst. The latter is an added advantage besides the cocatalyst properties. Moreover, the relatively lower cost of Ag nanoparticles favors their use as cocatalysts. Thus, Tsukamoto and colleagues reported the enhanced photocatalytic H₂O₂ generation on the Ag/TiO₂ composite.²⁶ This improvement was attributed to the plasmonic Ag cocatalyst, which generates photoexcited electrons with favorable redox potentials capable of efficiently reducing oxygen.²⁹

The current study investigates the photocatalytic H₂O₂ production activity on Ag-loaded starch functionalized magnetite (abbreviated as Ag/s-Fe₃O₄) composite nanoparticles. Note that photocatalytic H₂O₂ production on this composite has not been reported previously. The optical properties and band edges of the composite nanoparticles are thoroughly investigated. Their H₂O₂ production photocatalytic activity is compared to pristine Fe₃O₄ nanoparticles and Ag-loaded Fe₃O₄ nanoparticles (without starch functionalization). Photogenerated charge transfer and separation are examined using photoluminescence (PL) and electrochemical analysis. X-ray photoelectron spectroscopy (XPS) analyzed the chemical species and their oxidation states on the composite surface. Large-scale classical molecular dynamics (MD) simulations investigated the adsorption affinity of O₂ and H₂O molecules on the Fe₃O₄, s-Fe₃O₄, and Ag/s-Fe₃O₄ systems. Several control experiments and MD simulations were conducted to obtain insight into the photocatalytic H₂O₂ production mechanism.

2. Experimental section

2.1 Synthesis of starch-functionalized magnetite (s-Fe₃O₄)

A suitable volume of 0.4 M NaOH solution was heated at 80 °C. Then, an aqueous solution of FeSO₄·7H₂O (0.2M) and two wt% starch was added dropwise to it from the burette. The

temperature of the reaction mixture was maintained at 80 °C throughout this process, and the reaction was continued for 2 hours until the complete formation of a dark black precipitate. This precipitate was isolated *via* magnetic decantation and thoroughly washed multiple times with distilled water and ethanol until a neutral pH was achieved. Next, the washed precipitate was dried at 60 °C for 24 hours. This research publication uses the abbreviation s-Fe₃O₄ (starch-functionalized magnetite) for these nanoparticles. A sample of Fe₃O₄ nanoparticles, without starch, was also prepared using a similar synthesis protocol.

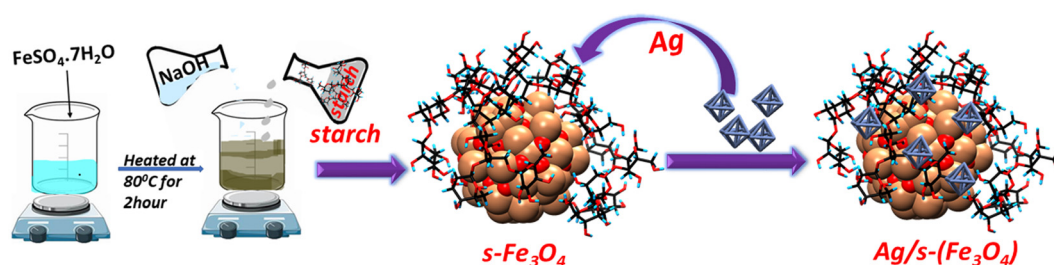
2.2 Synthesis of Ag-loaded s-Fe₃O₄

An appropriate amount of s-Fe₃O₄ nanoparticles was dispersed in distilled water by bath sonication for 30 minutes. Next, a calculated amount of AgNO₃ (5, 10, and 20 wt%) solution was added to the dispersed solution of s-Fe₃O₄. The aqueous dispersion was agitated in a shaker for 12 hours. Then, 1 wt% starch and 0.1 M glucose were added to the mixture and heated at 60 °C for one hour. The pH of the mixture was maintained carefully at ~8 by adding an appropriate amount of 0.2 M NaOH solution. Next, the prepared composite was separated magnetically, and the product was washed multiple times with distilled water (DW) and ethanol. The product was subsequently dried for 20 hours at 50 °C. Samples prepared were coded as 5Ag/s-Fe₃O₄, 10Ag/s-Fe₃O₄, and 20Ag/s-Fe₃O₄ based on the weight percent of AgNO₃ used in their preparation. Thus, 5, 10, and 20Ag represent the different weight percentages of silver loading on the s-Fe₃O₄. Additionally, one more sample, 10Ag/Fe₃O₄, was prepared using a protocol similar to the previous samples but without adding starch. It is labeled as 10Ag/Fe₃O₄, denoting ten-weight percent Ag loaded onto Fe₃O₄ nanoparticles. Scheme 1 illustrates the synthesis pathway for Ag/s-Fe₃O₄ photocatalysts.

2.3 Photocatalysis procedure

The photocatalyst sample (1 mg) was suspended in pure water or a sacrificial agent/water mixture (5/95%v/v; 12 ml) in a quartz tube. The tube was thoroughly sealed with a silicone rubber septum cap. Bath sonication was conducted for 10 minutes to ensure proper catalyst dispersion in the reaction mixture. Oxygen was bubbled into the suspension. Subsequently, the mixture was kept in the dark for 60 minutes to reach adsorption–desorption equilibrium. After that, the above-prepared mixture was photo-irradiated with visible light (cool white LED source; 1070 W m^{−2}) for 60 minutes. The photocatalyst nanocomposite particles were quickly recovered from the suspension by magnetic separation. The H₂O₂ production in the remaining aqueous solution was monitored by an iodometric method. H₂O₂ molecules react with excess iodide anions (I[−]) under acidic conditions (H₂O₂ + 3I[−] + 2H⁺ → I₃[−] + 2H₂O), producing triiodide anions (I₃[−]). The latter exhibits a significant absorption peak at approximately 350 nm. The quantity of I₃[−] was determined by interpolating the UV–visible absorbance at 350 nm in a standard H₂O₂ calibration plot.^{10,30,31} Separate photocatalytically produced H₂O₂





Scheme 1 The synthesis pathway of Ag/s-Fe₃O₄ photocatalysts.

measurement experiments were performed under similar conditions with pure water, 5 vol% isopropanol, 5 vol% ethanol, and 5 vol% glycerol aqueous suspensions.

2.4 Computational studies

We employed the material and process simulation software (MAPS 4.01 by Scienomics) to construct the molecular models for MD simulations. In this research, three simulations were conducted to study the interaction of H₂O₂ with Fe₃O₄, s-Fe₃O₄, and Ag/s-Fe₃O₄ clusters. An initial supercell model was built using an inverse spinel FCC unit cell of Fe₃O₄ (COD entry number: 907644). A nanocluster consisting of 149 atoms (Fe₆₉O₈₀) was constructed from the Fe₃O₄ supercell, with the diameter of this Fe₃O₄ nanocluster model measuring 1.4 nm. This Fe₃O₄ nanocluster was then placed in the center of a cubic simulation box measuring 40 Å × 40 Å × 40 Å in dimensions (Fig. S1a†).

The first step for modeling s-Fe₃O₄ was constructing an amylopectin unit composed of the C₂₄H₄₁O₂₁ molecular formula using the molecular builder plugin in MAPS software. The amylopectin unit was optimized by Modified Neglect of Diatomic Overlap (MNDO) using MAPS software. Then, five amylopectin units were positioned close to the above-constructed Fe₃O₄ nanocluster (Fig. S1b†). After initial optimization, an MD equilibration run of ~1 ns was used to adsorb the amylopectin onto the magnetite nanocluster surface. The resulting model of the starch-functionalized Fe₃O₄ nanocluster is named SFC. Similarly, the third model, Ag-loaded s-Fe₃O₄, was constructed. Initially, we carved a 0.6 nm Ag nanocluster with six atoms from an FCC Ag supercell. Subsequently, this Ag nanocluster was placed on the above-constructed s-Fe₃O₄ model (Fig. S1c†).

H₂O and O₂ molecules were constructed using the molecule builder plugin in MAPS and then optimized using the MNDO method. The H₂O molecules were further modified with simple point charge (SPC) in Dreiding force field. The SPC charges for water molecules for Hydrogen and Oxygen are given in Table S1 (ESI†). This study inserted 20 O₂ and 2000 H₂O molecules into the Fe₃O₄, s-Fe₃O₄, and Ag/s-Fe₃O₄ cubic cluster systems, hereafter called FC, SFC, and AgSFC models. The insertions maintained a fixed density of approximately 1.05 g cc⁻¹. Next, the conjugate gradient method was utilized to optimize the constructed simulation box. Following optimization, these models underwent MD simulations utilizing

MAPS's pre-installed LAMMPS (Large-scale Atomic Molecular Massively Parallel System) software. The MD simulations employed a modified 'Dreiding' force field. The potential energy contribution from non-bonded interactions in the 'Dreiding' force field was defined by the Lennard-Jones (LJ) 12-6 potential equation.³²

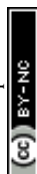
$$E_{ij}^{LJ} = 4\epsilon_0 \left[\left(\frac{\sigma_0}{r_{ij}} \right)^{12} - \left(\frac{\sigma_0}{r_{ij}} \right)^6 \right] \quad (1)$$

In eqn (1), ϵ_0 represents the potential well depth, σ_0 is the van der Waals radii, and r_{ij} is the interatomic distance between atom types i and j .

Table S2† gives the L-J parameters used in this research. Periodic boundary conditions were applied across all dimensions of the simulation cell. The temperature was maintained at room temperature ($T = 298.15$ K). MD simulations were conducted in the NVT ensemble over a ten-nanosecond (10 ns) period, employing a time step of one-femtosecond (1 fs). Coulomb interactions were computed using the particle mesh approach with a 12 Å cut-off distance.

3. Materials characterization

As-prepared photocatalysts' powder X-ray diffraction (XRD) patterns were captured on a Rigaku Miniflex 600 Desktop instrument (manufactured by RIGAKU Corporation). The device employed a Cu K α irradiation source (wavelength = 1.54 Å) with a scanning rate of 5° per minute and a step size of 0.01 while recording the patterns. A Tecnai G2 20 TWIN instrument (manufactured by EDAX Inc.) operating at an accelerating voltage of 200 kV was utilized for capturing transmission electron microscopy (TEM) images of different samples. The photocatalytic H₂O₂ production was measured spectrophotometrically by an iodometric method using an Agilent Cary 60 UV-vis spectrophotometer instrument. Solid-state UV-vis reflectance spectroscopy was performed using a UV-2600 spectrophotometer (Shimadzu; Japan) from 200 to 1000 nm. XPS was conducted using an ESCA M-Probe instrument with an Al K α source. The photoluminescence (PL) spectra of the samples were captured using a Hitachi F-4600 spectrophotometer with an excitation wavelength of 280 nm. The prepared powder samples' magnetic characteristics were analyzed using a Microsense (EZ9) vibrating sample magnetometer (VSM).



4. Results and discussion

Fig. 1 shows the XRD pattern of the as-prepared s-Fe₃O₄ and Ag/s-Fe₃O₄ photocatalyst. The characteristic diffraction pattern at scattering angles (2θ) of 18.33, 30.15, 35.51°, 37.15°, 43.2°, 53.56°, 57.12°, and 62.70° correspond to the Fe₃O₄ with (111), (220), (311), (222) (400), (422), (511), and (440) crystal planes, respectively (JCPDS no. 88-0315). Two distinct sets of cubic Ag and Fe₃O₄ diffraction peaks can be seen in the Ag/s-Fe₃O₄ sample. The diffraction peaks of Ag nanoparticles at 2θ values of 38.12° and 44.39° can be attributed to the (111) and (200) crystallographic planes, which is consistent with the standard XRD data for the cubic (FCC) phase Ag (JCPDS no. 89-3722). This indicates the successful formation of metallic Ag-loaded Fe₃O₄ nanoparticles.

Thermo-gravimetric analysis (TGA) was conducted on pure Fe₃O₄ and s-Fe₃O₄ samples to confirm the starch functionalization of Fe₃O₄ nanoparticles. The TGA was carried out at a heating rate of 5 °C min⁻¹ within 40 to 500 °C under a N₂ atmosphere. Fig. S2† illustrates the TGA curves of the pure Fe₃O₄ and s-Fe₃O₄ samples. The pure Fe₃O₄ nanoparticles displayed a weight loss of only 1.19 wt% due to the removal of adsorbed water molecules. In contrast, the TGA curve of the s-Fe₃O₄ sample exhibited two distinct decomposition steps. The initial weight loss, occurring between 50–150 °C, was ascribed to starch dehydration, while the subsequent loss, observed from around 200 °C to 500 °C, corresponded to its

thermal decomposition. The starch content in s-Fe₃O₄ was estimated to be 15.56% by weight.

Fig. 2 presents the TEM and HR-TEM images of pure Fe₃O₄, s-Fe₃O₄, and 10Ag/s-Fe₃O₄ nanoparticles. The TEM images reveal that pure Fe₃O₄ and s-Fe₃O₄ nanoparticles are mostly spherical (Fig. 2a and d). The HR-TEM image and inverse fast Fourier transform (IFFT) analysis of pure Fe₃O₄ in Fig. 2(b and c) indicate a *d*-spacing of 0.48 nm, corresponding to the (111) crystal plane of Fe₃O₄. The average particle size for pure Fe₃O₄ nanoparticles (Fig. 2a) is approximately 25–30 nm, while s-Fe₃O₄ nanoparticles (Fig. 2d) have an average size of 10–12 nm. Thus, starch capping reduces the size of Fe₃O₄ nanoparticles. Fig. 2e and f present the HRTEM image and IFFT analysis of the s-Fe₃O₄ photocatalyst, revealing a lattice fringe of 0.48 nm, which confirms the successful synthesis of starch-functionalized Fe₃O₄ nanoparticles.

Fig. 2g displays the TEM image of the 10Ag/s-Fe₃O₄ photocatalyst. The HR-TEM image and IFFT analysis of 10Ag/s-Fe₃O₄ photocatalyst in Fig. 2h and i display two adjacent regions with distinct lattice fringes 0.23 nm and 0.48 nm attributed to the (111) planes of Ag and the (111) planes of Fe₃O₄, indicating the formation of Ag/s-Fe₃O₄ nanostructures. Additionally, Fig. S3a† presents the TEM images of the 20Ag/s-Fe₃O₄ photocatalyst, which clearly shows a morphology similar to that of 10Ag/s-Fe₃O₄. However, the increased Ag loading from 10 to 20 wt% results in noticeable agglomeration and dense Ag coverage. Fig. 2j shows the elemental mapping of the 10Ag/s-Fe₃O₄ photocatalyst. It reveals the homogeneous distribution of Fe, O, and Ag elements in a specific region within the SEM micrograph of the 10Ag/s-Fe₃O₄ photocatalyst sample. Furthermore, the Energy Dispersive X-ray Spectroscopy (EDS) data confirms that all elements (Fe, O, and Ag) are present in the sample in the expected stoichiometric proportions (Fig. S3b and c†).

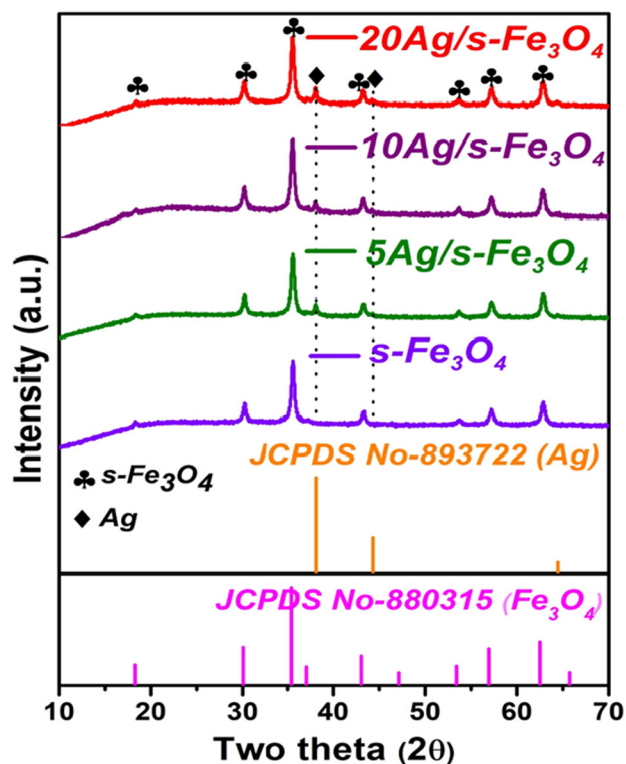


Fig. 1 XRD patterns of pure s-Fe₃O₄ and different wt% of Ag-loaded s-Fe₃O₄ photocatalysts.

4.1 Optical properties

The solid-state UV-visible absorption spectra of the as-prepared photocatalysts are depicted in Fig. 3a. It is observed that the absorption edge of the Ag-loaded s-Fe₃O₄ samples falls within a similar range of visible wavelengths as the s-Fe₃O₄ catalyst. The optical band gaps of Fe₃O₄, s-Fe₃O₄, and Ag-loaded s-Fe₃O₄ photocatalysts were determined from the Tauc plots (derived from the Kubelka–Munk equation).^{33,34}

$$(\alpha h\nu)^{1/n} = A(h\nu - E_g) \quad (2)$$

Here, α represents the absorption coefficient, h represents Planck's constant, ν is the light frequency, A denotes the proportionality constant, and E_g is the band-gap energy.

The Tauc plots (Fig. 3b) reveal that the band gaps of pure Fe₃O₄, s-Fe₃O₄, and Ag-loaded Fe₃O₄ (5, 10, 20 wt%) are 1.87, 2.28, and 2.28 eV, respectively. Moreover, it is observed that the band gap of Fe₃O₄ (1.87 eV) is enhanced after functionalization with starch due to the smaller particle size (quantum size effect) of the s-Fe₃O₄ sample (2.28 eV). Fig. 3c depicts the UV-visible absorbance spectra of aqueous sols of s-Fe₃O₄, 5Ag/s-Fe₃O₄,



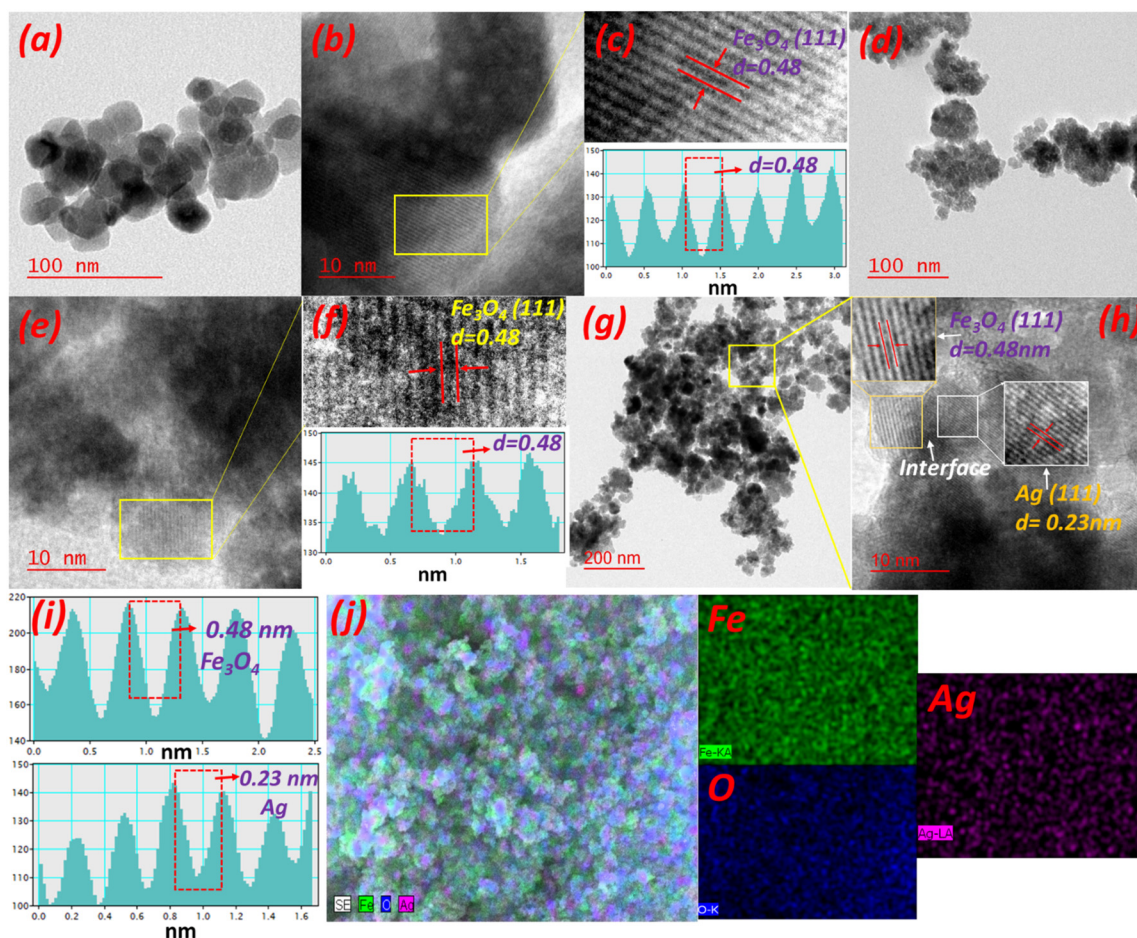


Fig. 2 TEM, HR-TEM, and IFFT analysis of (a–c) pure Fe_3O_4 photocatalyst, (d–f) $s\text{-Fe}_3\text{O}_4$ photocatalyst, and (g–i) $10\text{Ag/s-Fe}_3\text{O}_4$ photocatalyst. (j) SEM images and corresponding elemental mapping of the $10\text{Ag/s-Fe}_3\text{O}_4$ photocatalyst.

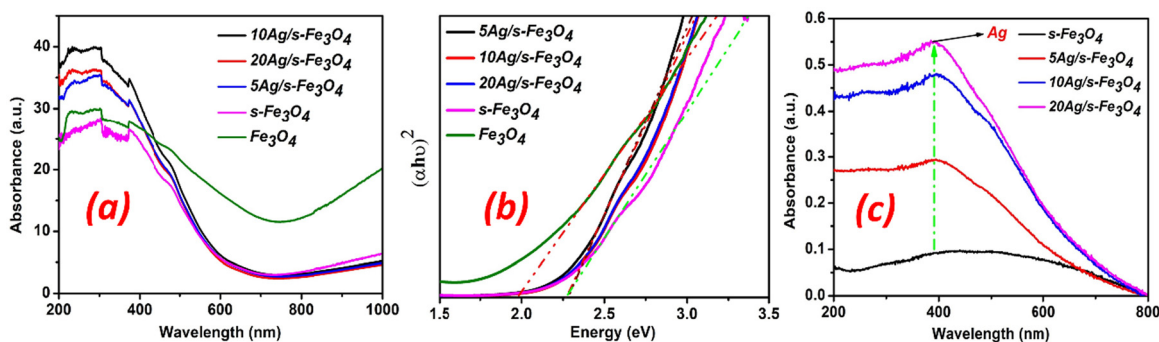


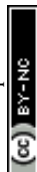
Fig. 3 (a) The solid-state UV absorbance spectra of the as-prepared photocatalyst, (b) the Tauc plot, and (c) the UV-visible absorbance spectra of aqueous sols of the nanoparticle samples.

$10\text{Ag/s-Fe}_3\text{O}_4$, and $20\text{Ag/s-Fe}_3\text{O}_4$ nanoparticles. Compared to the $s\text{-Fe}_3\text{O}_4$ photocatalyst, Ag nanostructures loaded on the $s\text{-Fe}_3\text{O}_4$ surface present stronger visible light absorption. The absorption peak at 395 nm corresponds to the LSPR absorbance of metallic Ag nanostructures on the $\text{Ag/s-Fe}_3\text{O}_4$ photocatalysts.

The PL spectra were acquired for $s\text{-Fe}_3\text{O}_4$ and $10\text{Ag/s-Fe}_3\text{O}_4$ using photoexcitation at 350 nm. As shown in Fig. S4a,† the PL

emission intensity decreases upon incorporating silver up to 10 wt% ($10\text{Ag/s-Fe}_3\text{O}_4$). The lower PL emission intensity of the $10\text{Ag/s-Fe}_3\text{O}_4$ sample compared to the $s\text{-Fe}_3\text{O}_4$ photocatalyst suggests that it has the slowest electron–hole recombination, leading to higher photocatalytic capability.³⁵

FTIR was employed to understand the interaction of starch and Fe_3O_4 nanoparticles. Fig. S5 (ESI†) presents the FTIR



spectra of Fe_3O_4 (without starch) and $\text{s-Fe}_3\text{O}_4$ (starch functionalized) samples. In the FTIR spectrum of the $\text{s-Fe}_3\text{O}_4$ sample, distinct peaks are observed at 2926, 1156, and 1032 cm^{-1} , matching the stretching frequencies related to C–H, glycosidic C–O–C, and C–O bonds, respectively. As anticipated, these peaks are absent from the FTIR spectrum of the Fe_3O_4 sample (before starch functionalization). The latter again confirms the successful preparation of starch-functionalized Fe_3O_4 nanoparticles. The absorption peak at approximately 3430 cm^{-1} is associated with vibrations corresponding to the stretching mode of O–H bonds. The signals at 1641 cm^{-1} and 582 cm^{-1} correspond to the hydroxyl groups on the surface of the H_2O molecule and Fe–O stretching vibrations.^{36,37}

4.2 Electrochemical analysis

Fig. 4a presents the electrochemical impedance spectroscopy (EIS) of $\text{s-Fe}_3\text{O}_4$ and different wt% of Ag-loaded $\text{s-Fe}_3\text{O}_4$ photocatalysts, while the accompanying inset depicts the corresponding equivalent circuit model used for analysis. The parameters R_{ct} and R_s represent the charge transfer resistance and electrolyte solution resistance, within the equivalent circuit model, respectively. The Ag-loaded $\text{s-Fe}_3\text{O}_4$ samples exhibit a smaller arc radius than pure $\text{s-Fe}_3\text{O}_4$, indicating reduced charge transfer resistance. Among all the photocatalysts, the 10Ag/ $\text{s-Fe}_3\text{O}_4$ sample demonstrates the smallest arc radius, demonstrating lower charge transfer resistance and superior charge separation in this composite.³⁸ This is consistent with this sample's enhanced photocatalytic performance and lowest PL intensity observations. Fig. S4b† illustrates the visible-light-induced photocurrent responses of the $\text{s-Fe}_3\text{O}_4$, 10Ag/ $\text{s-Fe}_3\text{O}_4$ samples for multiple on–off cycles. The significantly improved photocurrent density of 10Ag/ $\text{s-Fe}_3\text{O}_4$ under light exposure provided evidence for efficient charge carrier mobility resulting from the proper interface of the metallic Ag with $\text{s-Fe}_3\text{O}_4$ photocatalyst. Additionally, the enhanced photocurrent density in the 10Ag/ $\text{s-Fe}_3\text{O}_4$ composite can be attributed to the effective suppression of recombination among photogenerated

charge carriers, which occurs due to the increased lifespan of excitons.³⁸

The Mott–Schottky (MS) plots of the samples were analyzed to determine the semiconductor type and flat band potential of the synthesized photocatalysts.³⁹ These plots (Fig. 4b) exhibit positive slopes, showing that $\text{s-Fe}_3\text{O}_4$ nanoparticles are n-type semiconductors. The x-axis intercept of the fits to the linear portions of these MS plots shows that the CB positions of $\text{s-Fe}_3\text{O}_4$ nanoparticles are 0.28 V, respectively. The MS results are combined with the band gap values of $\text{s-Fe}_3\text{O}_4$ (using the equation $E_{\text{CB}} = E_{\text{VB}} - E_{\text{g}}$) to calculate respective VB positions.⁴⁰ Consequently, the VB positions are 2.56 V for $\text{s-Fe}_3\text{O}_4$. The following relationship is employed: $V(\text{NHE}) = V(\text{Ag}/\text{AgCl}) + 0.059 \times \text{pH} + 0.197$ to convert potential measurements from the Ag/AgCl reference electrode scale to the NHE scale for all electrochemical assessments.^{41,42}

The elemental compositions and surface electronic environment of the $\text{s-Fe}_3\text{O}_4$ and 10Ag/ $\text{s-Fe}_3\text{O}_4$ photocatalysts were examined by XPS. Fig. S6† demonstrates the XPS survey spectra of the $\text{s-Fe}_3\text{O}_4$ and 10Ag/ $\text{s-Fe}_3\text{O}_4$ samples, revealing the elemental composition of the prepared sample. This analysis confirms the presence of Fe, O, and C in $\text{s-Fe}_3\text{O}_4$ and Fe, O, C, and Ag elements in the 10Ag/ $\text{s-Fe}_3\text{O}_4$ samples. Fig. 5(a–c) compares the high resolution (HR) XPS of Fe 2p and O 1s elements in pristine $\text{s-Fe}_3\text{O}_4$ with the same species in 10Ag/ $\text{s-Fe}_3\text{O}_4$ sample. Fig. 5a shows the HR XPS of Fe 2p spectra for pristine $\text{s-Fe}_3\text{O}_4$ and 10Ag/ $\text{s-Fe}_3\text{O}_4$ samples. Fe 2p_{3/2} and Fe 2p_{1/2} peaks at binding energies (BE) of 709.12 eV and 722.6 eV, respectively, in the $\text{s-Fe}_3\text{O}_4$ sample, indicating the presence of Fe^{3+} and Fe^{2+} species. Furthermore, the presence of a satellite peak at 716.8 eV and 731.6 eV also suggests the coexistence of Fe^{2+} and Fe^{3+} (Fig. 5a).⁴³ The Fe 2p_{3/2} and Fe 2p_{1/2} peaks show a positive shift to 710.3 and 723.8 eV in the XPS of the 10Ag/ $\text{s-Fe}_3\text{O}_4$ sample (Fig. 5a). The HR XPS spectra of O 1s in pure $\text{s-Fe}_3\text{O}_4$ and 10Ag/ $\text{s-Fe}_3\text{O}_4$ samples are shown in Fig. 5b. The three fitted distinctive peaks of O 1s at BE of 529.3, 531, and 532.2 are attributed to the Fe–O (lattice oxygen), hydroxyl, and

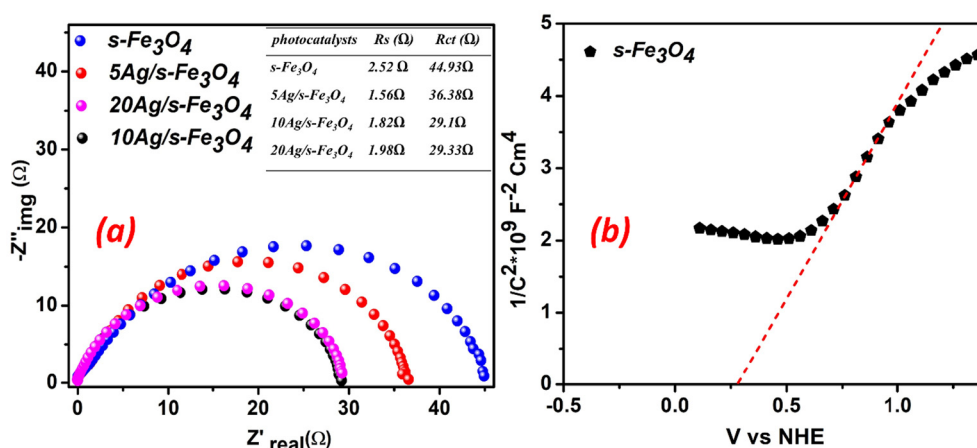


Fig. 4 (a) Nyquist plots of pure $\text{s-Fe}_3\text{O}_4$ and different (wt% of) Ag-loaded $\text{s-Fe}_3\text{O}_4$ photocatalysts and (b) Mott–Schottky plots for $\text{s-Fe}_3\text{O}_4$ photocatalyst.



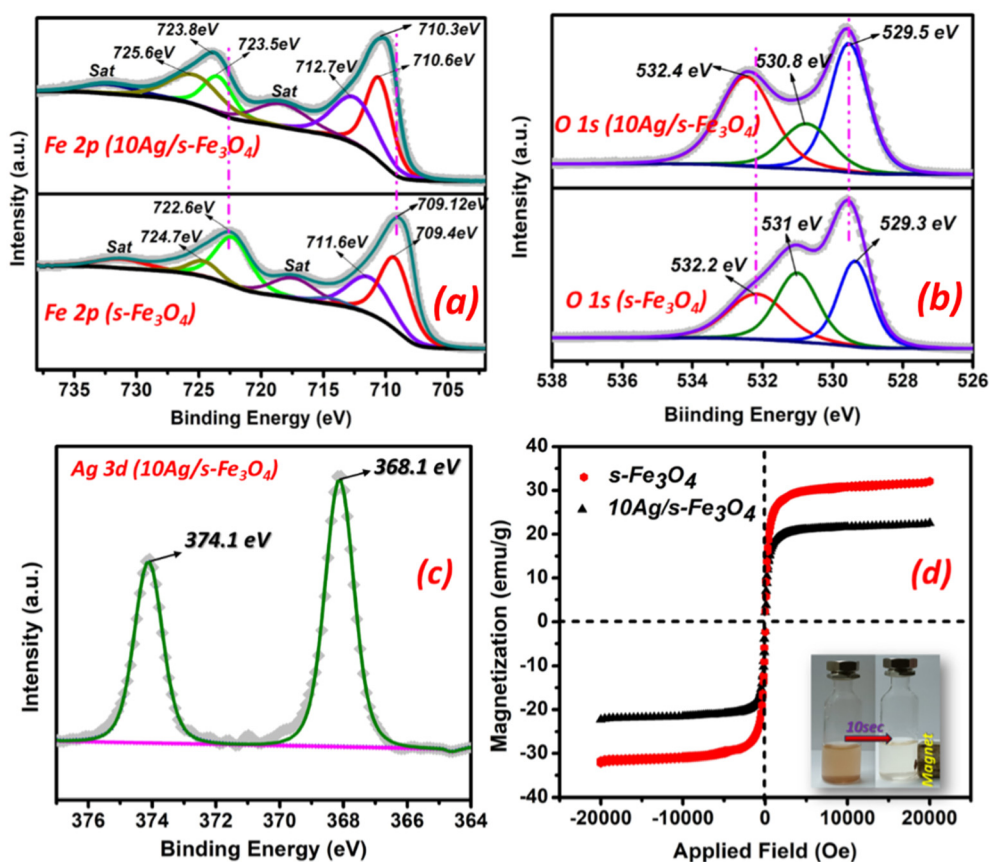


Fig. 5 XPS spectra of (a) Fe 2p of $s\text{-Fe}_3\text{O}_4$ and $10\text{Ag}/s\text{-Fe}_3\text{O}_4$, (b) O 1s of $s\text{-Fe}_3\text{O}_4$ and $10\text{Ag}/s\text{-Fe}_3\text{O}_4$, (c) Ag 3d of $10\text{Ag}/s\text{-Fe}_3\text{O}_4$ photocatalyst. (d) Magnetization versus applied magnetic field plots of $s\text{-Fe}_3\text{O}_4$ and $\text{Ag}/s\text{-Fe}_3\text{O}_4$ photocatalysts. The inset picture is of an aqueous dispersion of photocatalyst nanoparticles before and after magnetic separation.

surface adsorbed oxygen.^{44,45} These peaks shift to 529.5, 530.8, and 532.4 eV in the $10\text{Ag}/s\text{-Fe}_3\text{O}_4$ sample.

The Ag 3d spectrum in Fig. 5c displays two distinct peaks at 368.1 eV and 374.1 eV. These two peak locations correspond to the BE for Ag $3d_{3/2}$ and Ag $3d_{5/2}$, respectively, which point to the presence of metallic silver (Ag^0).⁴⁶ Additionally, the positive BE shift in the Fe 2p and O 1s peak positions in $10\text{Ag}/s\text{-Fe}_3\text{O}_4$ compared to $s\text{-Fe}_3\text{O}_4$ photocatalyst indicates charge transfer from $s\text{-Fe}_3\text{O}_4$ nanoparticles to metallic Ag. It also demonstrates the chemical interaction between Ag metals and $s\text{-Fe}_3\text{O}_4$ nanoparticles at the interface of the nanostructures.^{47,48}

Fig. 5d shows the magnetization versus magnetic field (M-H) curves of $s\text{-Fe}_3\text{O}_4$ and $10\text{Ag}/s\text{-Fe}_3\text{O}_4$ photocatalyst in the $-20 \text{ kOe} < H < +20 \text{ kOe}$ range at room temperature (300 K). The photocatalysts $s\text{-Fe}_3\text{O}_4$ and $10\text{Ag}/s\text{-Fe}_3\text{O}_4$ demonstrated saturation magnetization (M_s) values of 31.5 and 22.6 emu g^{-1} , respectively. The S-shaped M-H curve with negligible hysteresis showed that the prepared nanoparticle samples were superparamagnetic.^{49,50} These magnetic properties facilitate efficient magnetic separation of the photocatalyst when subjected to an external magnetic field. The inset image in the figure shows that the photocatalyst nanoparticles can be separated within 10 seconds using an external magnetic field.

4.3 MD results

Fig. 6(a-c) depicts the FC, SFC, and AgSFC system's snapshot at the end of a 10 ns equilibration run. The figures illustrate the distribution of O_2 and H_2O molecules surrounding Fe_3O_4 , $s\text{-Fe}_3\text{O}_4$, and $\text{Ag}/s\text{-Fe}_3\text{O}_4$ units. However, this depiction lacks quantitative insight into the probability of O_2 and H_2O positions relative to the photocatalysts Fe_3O_4 , $s\text{-Fe}_3\text{O}_4$, and $\text{Ag}/s\text{-Fe}_3\text{O}_4$ clusters. The snapshot of the $\text{Ag}/s\text{-Fe}_3\text{O}_4$ model in Fig. 6c clearly shows the adsorption of O_2 molecules on the Ag nanocluster (denoted by the green circle).

The intermolecular Radial Distribution Function (RDF) plots depicted in Fig. 7 elucidate the nature of interactions between different atom types comprising the FC, SFC, and AgSFC systems. RDF gives the atom type to atom type most probable distance. The RDF plots probe the molecular associations between iron (Fe) and oxygen (O) atoms in the Fe_3O_4 nanocluster with atom types making O_2 and H_2O molecules. Table 1 details the atom-type nomenclature used across all figures (Table 1) illustrating MD simulation results. The first interaction peak emerges at approximately 2.7 Å in the RDF of the FC. It demonstrates significant interaction between Fe atoms of Fe_3O_4 and O atoms of O_2 molecules. Another peak in



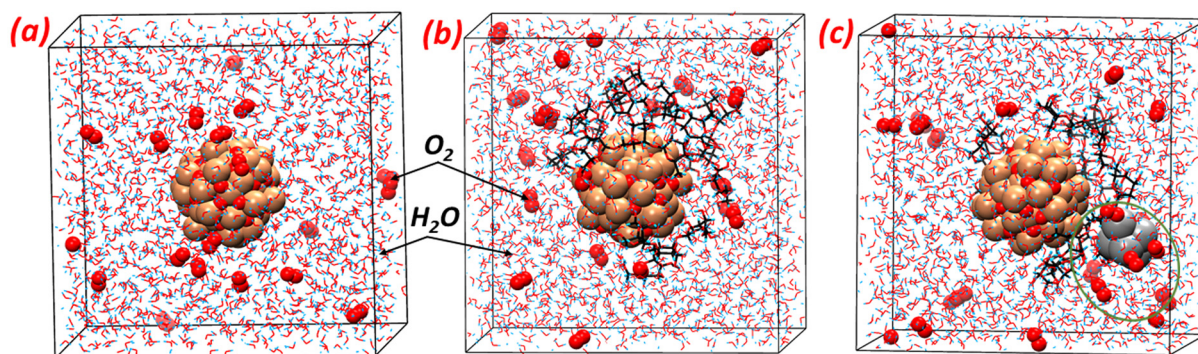


Fig. 6 shows a snapshot of the simulated system. (a) FC model (b) SFC model (c) AgSFC.

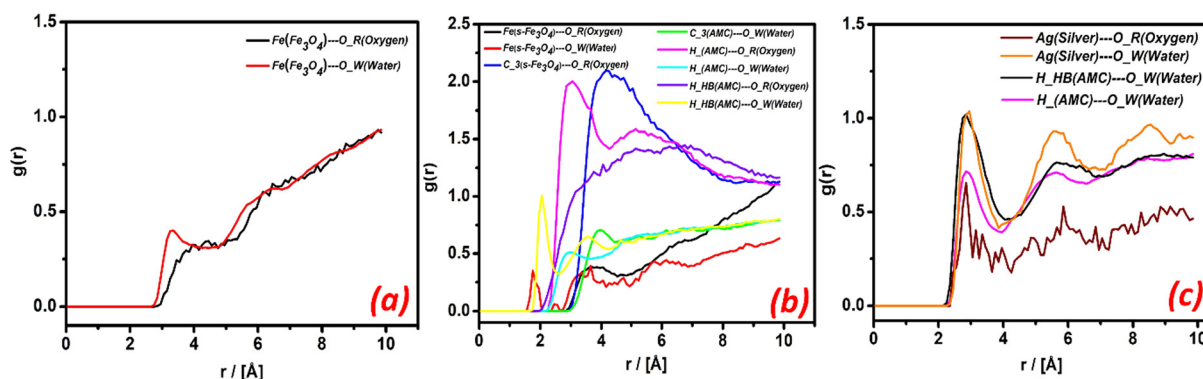


Fig. 7 RDF ($g(r)$) vs. distance of interaction $r/[\text{\AA}]$. (a) FC model (b), SFC model (c), and AgSFC model.

Table 1 The naming convention used in the RDF plots is as follows

Atom type	Meaning
Fe	The iron atom in Fe_3O_4
O_R	Oxygen atom in the O_2 molecule
O_W	Oxygen atom in the H_2O molecule
Ag	The silver atom of the Ag cluster
H_HB	Hydrogen atom is bonded to an oxygen atom in the amylopectin
H_	The hydrogen atom is bonded to the carbon atom in the amylopectin
C_3	The carbon atom in amylopectin

Fig. 7a, which occurs at 2.9 Å, is between the Fe atoms of Fe_3O_4 and the O atoms of H_2O molecules.

Fig. 7b shows the SFC (RDF) plots between atom types in s- Fe_3O_4 and those in O_2 and H_2O molecules. Notably, amylopectin (AMC) molecules are partially adsorbed onto the Fe_3O_4 nanocluster, leading to intermolecular interactions between AMC atom types (e.g., C and H) and the O atoms of both O_2 and H_2O molecules. The H_HB atoms of AMC in the s- Fe_3O_4 system display strong interaction peaks around 1.7 Å and 2.07 Å due to interactions between H_HB...O_W and H_HB...O_R. Similarly, two other peaks of H_ atoms of AMC in the s- Fe_3O_4 system show interactions between H_...O_R and

H_...O_W at approximately 2.3 Å. The C_3 atoms of AMC in the s- Fe_3O_4 system also show interactions with O_W and O_R at a similar peak distance of 3 Å. The Fe atoms of the s- Fe_3O_4 system display notable peak intensities for Fe...O_W and Fe...O_R at 1.56 Å and 2.9 Å, respectively.

Prominent peaks in the AgSFC systems (Fig. 7c) demonstrate that Ag has a strong interaction with the O_R atom type in the 2.5 to 3 Å range. The Ag atom type also interacts with the O_W atom type at a similar distance. At the same distance, there is also a strong interaction between the amylopectin H_HB and the O_W atom types. Furthermore, Fig. S7 in the ESI† illustrates the atom-type interactions in the AgSFC model, specifically between Fe and O_W, as well as between C_3 (AMC) and both O_R and O_W. Thus, functionalizing Fe_3O_4 with starch (SFC system) enhances water adsorption affinity, and incorporating Ag onto s- Fe_3O_4 (AgSFC system) increases O_2 adsorption affinity.

4.4 Photocatalytic H_2O_2 production activity

No H_2O_2 production was detected on the prepared photocatalysts under dark conditions. Subsequently, all samples' photocatalytic activities for H_2O_2 production were evaluated under visible light irradiation using only water at neutral pH. The pristine Fe_3O_4 and s- Fe_3O_4 (without silver loading) nanoparticles showed inefficient H_2O_2 production due to poor



visible light absorption and quick photoinduced charge carrier recombination. A considerable amount of H_2O_2 formation was detected from pure water following 60 minutes of visible light exposure at a neutral pH on Ag-loaded $\text{s-Fe}_3\text{O}_4$ nanostructures. The H_2O_2 production on $10\text{Ag/s-Fe}_3\text{O}_4$ was calculated to be $167\ \mu\text{mol g}^{-1}\ \text{h}^{-1}$ and ~ 16 times higher than that of $\text{s-Fe}_3\text{O}_4$. The 10 wt% Ag loading on the $\text{s-Fe}_3\text{O}_4$ nanostructure photocatalyst exhibits optimal photocatalytic H_2O_2 production activity at 60 min light exposure. However, when the Ag nanoparticle loading on $\text{s-Fe}_3\text{O}_4$ exceeds 10 wt%, the H_2O_2 formation rate decreases to $157\ \mu\text{mol g}^{-1}$. This reduction is attributed to agglomeration and excessive surface coverage at higher Ag loading (20 wt%), which can block active sites, hinder light penetration, and introduce recombination centers, ultimately reducing the photocatalytic activity. This is supported by the TEM image of the $20\text{Ag/s-Fe}_3\text{O}_4$ sample (Fig. S3a, ESI[†]), which clearly shows agglomeration and dense Ag coverage. Fig. 9a indicates that the $10\text{Ag/Fe}_3\text{O}_4$ photocatalyst, without starch functionalization, also exhibited an H_2O_2 generation rate of $83\ \mu\text{mol g}^{-1}\ \text{h}^{-1}$. This value is almost half the H_2O_2 generation rate observed for the $10\text{Ag/s-Fe}_3\text{O}_4$ (starch functionalized) photocatalyst. This comparison suggests that the starch-functionalized Ag-loaded Fe_3O_4 ($10\text{Ag/s-Fe}_3\text{O}_4$) photocatalyst significantly enhances its photocatalytic activity for H_2O_2 production. Starch functionalization on Fe_3O_4 makes its surface considerably more hydrophilic, demonstrating strong water adsorption. The increase in photocatalyst surface hydrophilicity likely improves the water oxidation efficiency, resulting in a higher H_2O_2 generation rate.

To explore the surface properties of the synthesized Fe_3O_4 , $\text{s-Fe}_3\text{O}_4$, and $10\text{Ag/s-Fe}_3\text{O}_4$ photocatalysts, the water contact angle (WCA) was measured on a pellet of each photocatalyst (Fig. 8). A decrease in the WCA indicates strong material adsorption (hydrophilicity). Pure Fe_3O_4 (without starch) displays a contact angle of 52.95° , highlighting its poor water adsorption (hydrophobic) nature (Fig. 8a). Following the functionalization with starch and Ag loading on Fe_3O_4 , the resulting photocatalysts, $\text{s-Fe}_3\text{O}_4$ and $10\text{Ag/s-Fe}_3\text{O}_4$, exhibit calculated contact angles of 26° and 25.2° , respectively, indicating an enhancement in hydrophilic properties (Fig. 8b and c). These findings demonstrate that the improved hydrophilicity

of $10\text{Ag/s-Fe}_3\text{O}_4$ promotes more efficient water oxidation. This also leads to longer residence times for solvent molecules, improving their interaction with photocatalyst particles and reactants.⁵¹

The photocatalytic experiments were conducted under four different pH conditions (pH 2, 3, 5, and 7) to investigate the influence of pH on H_2O_2 generation. The results revealed that the photocatalytic H_2O_2 production was significantly affected by the pH of the aqueous solution. Fig. 9b shows that $10\text{Ag/s-Fe}_3\text{O}_4$ exhibited the highest photocatalytic activity for H_2O_2 production at pH 3 ($258.7\ \mu\text{mol g}^{-1}\ \text{h}^{-1}$) compared to the other three pH values. This observation suggests that excess protons at pH 2 might gradually oxidize the produced H_2O_2 into H_2O ($\text{H}_2\text{O}_2 + 2\text{H}^+ + 2\text{e}^- = 2\text{H}_2\text{O}$). Conversely, in a less proton-rich environment at pH 5 and 7, the H_2O_2 production was lower due to faster H_2O_2 decomposition.³⁰ Consequently, a pH value of 3 was optimal for photocatalytic H_2O_2 production.

To gain more insight, additional controlled experiments were conducted to investigate how different gas environments (air, O_2 , and N_2) affect the photocatalytic activity of the $10\text{Ag/s-Fe}_3\text{O}_4$ photocatalyst in H_2O_2 production (Fig. 9c). The findings indicate that substituting O_2 with N_2 leads to a notable inhibition of the photocatalytic efficiency in the ORR, emphasizing the crucial role of dissolved O_2 during the ORR to H_2O_2 production process. To compare the results, photocatalytic tests were also conducted with different sacrificial agents (ethanol, IPA, and glycerol) on $10\text{Ag/s-Fe}_3\text{O}_4$ photocatalyst to determine whether these electron donor molecules could speed up the formation of H_2O_2 . Adding 5-vol% glycerol in water enhances (~ 2.5 times) the formation of H_2O_2 compared to pure water at pH 3. Fig. 9d compares the photocatalytic H_2O_2 formation activity on a $10\text{Ag/s-Fe}_3\text{O}_4$ sample with different sacrificial agents after 60 minutes of visible light irradiation. Additionally, Fig. 9h compares the results of photocatalytic H_2O_2 production of $10\text{Ag/s-Fe}_3\text{O}_4$ with other reported photocatalysts under different sacrificial agents in recent years. The detailed information on the previously reported photocatalysts is mentioned in Table S3 (ESI[†]).

The photocatalytic H_2O_2 formation experiment was repeated eight times to examine the long-term stability of

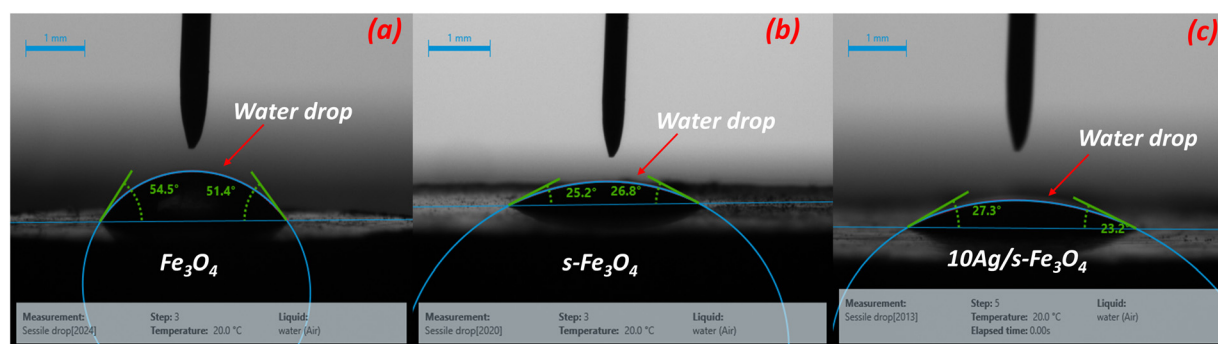


Fig. 8 Contact angle measurement on (a) Fe_3O_4 , (b) $\text{s-Fe}_3\text{O}_4$, and (c) $10\text{Ag/s-Fe}_3\text{O}_4$ photocatalysts.



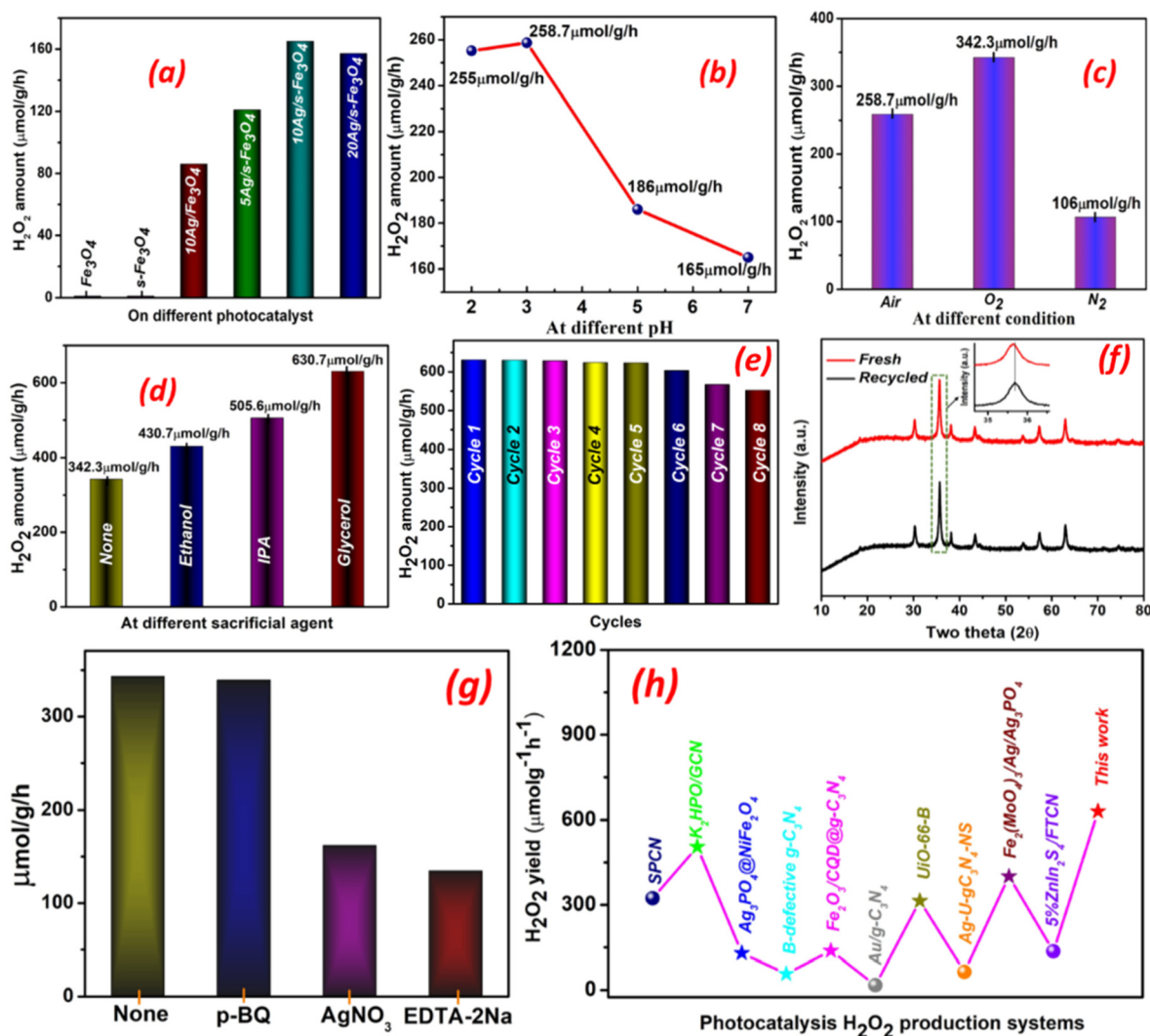


Fig. 9 (a) H_2O_2 production on different samples from pure water at neutral pH (b) H_2O_2 production at different pH on $10\text{Ag/s-Fe}_3\text{O}_4$ photocatalyst (c) H_2O_2 production at different conditions on $10\text{Ag/s-Fe}_3\text{O}_4$ photocatalyst (d) H_2O_2 production using different sacrificial agents on $10\text{Ag/s-Fe}_3\text{O}_4$ photocatalyst (e) recyclability performance on $10\text{Ag/s-Fe}_3\text{O}_4$ photocatalyst (f) XRD of recycled photocatalyst ($10\text{Ag/s-Fe}_3\text{O}_4$) (g) effect of different trapping agent on photocatalytic H_2O_2 production on $10\text{Ag/s-Fe}_3\text{O}_4$ photocatalyst (h) comparison data for photocatalytic H_2O_2 production with other previously reported photocatalysts in recent works.

the $10\text{Ag/s-Fe}_3\text{O}_4$ catalyst further. After each cycle, the photocatalyst was rinsed with distilled water and subsequently separated from the solution *via* magnetic decantation. The recovered sample was then reused for the next reaction cycle. The recyclability results show that the photocatalytic performance remains stable, with around a 13% reduction observed after the 8th cycle, indicating good long-term durability of the photocatalyst, as shown in Fig. 9e. Additionally, to evaluate the stability of the $10\text{Ag/s-Fe}_3\text{O}_4$ photocatalyst after photocatalytic cycles, XRD, TEM, and UV-visible spectroscopy analyses were performed on the recycled sample. The XRD pattern (Fig. 9f) shows no significant changes, indicating that the crystal structure remains largely intact. A very minor shift in the diffraction peaks was observed, which can be attributed to surface

oxygen passivation. TEM analysis (Fig. S8a†) was conducted to assess any morphological changes after recycling. The images confirm that the photocatalyst retains its structural integrity, with no noticeable aggregation of Ag nanoparticles, demonstrating good morphological stability. Furthermore, UV-Visible absorption spectra of the fresh and recycled samples (Fig. S8b†) show that the characteristic plasmonic peak of Ag nanoparticles, typically observed around 395 nm, remains unchanged after repeated photocatalytic cycles. This stable plasmonic response suggests negligible Ag leaching during the reaction. These results collectively confirm that the $10\text{Ag/s-Fe}_3\text{O}_4$ photocatalyst exhibits excellent structural and photochemical stability, making it highly suitable for efficient and repeated H_2O_2 generation under photocatalytic conditions.

5. Photocatalytic H₂O₂ production mechanism

The schematic in Fig. 10 proposes a possible photocatalytic H₂O₂ formation on the Ag/s-Fe₃O₄ photocatalyst. The series of experiments and MD simulation results facilitated the development of this mechanism. The experimental results show that photocatalytic H₂O₂ production activity increases substantially on the 10Ag/s-Fe₃O₄ photocatalyst compared to pristine and different Ag-loaded s-Fe₃O₄. The EIS, PL, and photocurrent results indicate that charge separation on the 10Ag/s-Fe₃O₄ photocatalyst reduces the likelihood of charge carrier recombination.

Active species trapping experiments were conducted using *p*-benzoquinone (PBQ), AgNO₃, and ethylenediamine tetraacetic acid disodium (EDTA-2Na) as scavengers for superoxide radicals ([•]O₂[−]), electrons (e[−]), and a hole scavenger, respectively. As shown in Fig. 9g, there is a significant decrease in H₂O₂ yield when AgNO₃ and EDTA-2Na are employed as scavenger agents, which means that e[−] and h⁺ play a crucial role in the oxygen reduction and water oxidation reaction. The performance of H₂O₂ production remains unaffected by the addition of PBQ, indicating superoxide radicals are not the active species for photocatalytic H₂O₂ generation. The formation of the [•]O₂[−] in the photocatalytic reaction is further examined by the nitro blue tetrazolium test (NBT). Fig. S9† depicts the absorption peak intensity of the NBT solution at 262 nm. Following the photocatalytic reaction, no alterations were noted in the absorption peak of the NBT solution, confirming that [•]O₂[−] does not serve as an active species in reducing O₂ to produce H₂O₂.

The photocatalytic activity is directly affected by the effective adsorption of reactants, particularly water and oxygen. Therefore, it is vital to consider H₂O and O₂ adsorption on the photocatalyst surface in aqueous conditions. As

illustrated by the MD simulation results, water adsorption predominantly takes place on the s-Fe₃O₄ surface, and oxygen adsorption takes place on the Ag of the Ag/s-Fe₃O₄ nanostructure. Starch functionalization of the Fe₃O₄ improves its hydrophilicity, which is necessary for efficient water oxidation. WCA measurements show that the 10Ag/s-Fe₃O₄ photocatalytic system has maximum water adsorption affinity.

The visible light illumination of the Ag/s-Fe₃O₄ photocatalysts photo-excited electrons from the VB of the s-Fe₃O₄ component. The H₂O molecules got oxidized by photo-generated holes in the VB of the photocatalyst and generated the H⁺ and O₂. Note that the VB position of s-Fe₃O₄ is 2.56 V vs. NHE, providing sufficient overpotential for water oxidation (1.23 V vs. NHE). H₂O₂ concentrations of 258.7 μmol g^{−1} h^{−1} and 106 μmol g^{−1} h^{−1} were maintained without an external O₂ supply. This observation indicates that O₂ is generated through water oxidation. Moreover, adding a suitable sacrificial agent (such as ethanol, IPA, or glycerol) significantly boosts H₂O₂ production by promoting its activation. This enhancement occurs as photogenerated holes are effectively scavenged through the oxidation of the sacrificial agent. Additionally, this process generates H⁺ ions, which subsequently react with adsorbed O₂ *via* the 2e[−] ORR to produce H₂O₂ (O₂ + 2H⁺ + 2e[−] → H₂O₂).

6. Conclusions

An efficient, visible-light-driven, and magnetically recyclable photocatalyst (Ag/s-Fe₃O₄) for H₂O₂ production was successfully synthesized using a two-step precipitation method. Fine Ag nanostructures were deposited on starch-functionalized Fe₃O₄ nanoparticle surfaces, where starch functionalization played a crucial role in preventing nanoparticle aggregation and reducing their size. Furthermore, water contact angle (WCA) measurements confirmed that starch functionalization enhances water wettability, making the photocatalyst surface more hydrophilic. MD simulations revealed that Ag loading on s-Fe₃O₄ enhances O₂ adsorption, while starch improves water molecule adsorption. The increased O₂ adsorption on Ag nanostructures is well known for facilitating oxygen reduction *via* the two-electron pathway, leading to efficient H₂O₂ production. Additionally, scavenger experiments confirmed that photocatalytic H₂O₂ production over Ag/s-Fe₃O₄ occurs through the two-electron O₂ reduction pathway. The Ag loading on s-Fe₃O₄ was optimized, with 10 wt% Ag deposition exhibiting the highest photocatalytic H₂O₂ production activity. However, excessive Ag deposition (20 wt%) reduced photocatalytic performance by covering the active sites on the s-Fe₃O₄ surface, while 5 wt% Ag loading resulted in poor charge transfer efficiency. The combined experimental and molecular dynamics study provides valuable insights for designing efficient photocatalysts for H₂O₂ production *via* the two-electron O₂ reduction pathway. This investigation highlights the significance of concurrent water adsorption on the

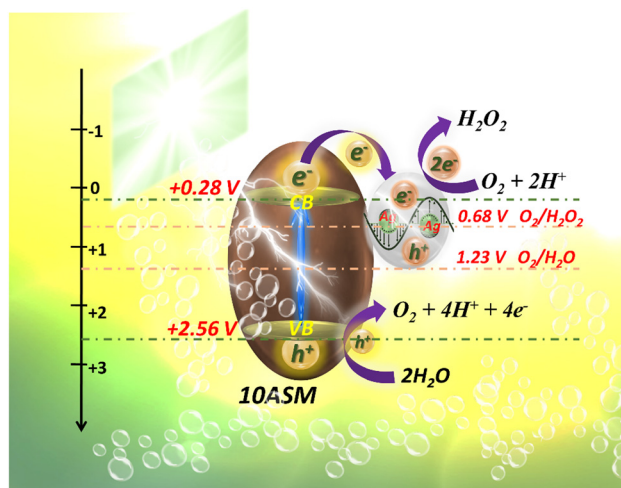


Fig. 10 Proposed mechanism for photocatalytic H₂O₂ production on 10Ag/s-Fe₃O₄.



VB part and oxygen interaction with the CB part of the photocatalyst for designing effective H₂O₂-producing photocatalysts.

Conflicts of interest

There are no conflicts to declare.

Data availability

Data are available upon request from the authors.

Acknowledgements

The authors gratefully acknowledge the financial support provided by BRNS (BARC, DAE) under the sponsored project (Sanction No. 58/14/18/BRNS-2019). We also acknowledge the Central Instrument Facility at IIT (BHU) for material characterization support. Additionally, the authors thank the PARAM Shivay facility at IIT (BHU) for providing computational resources under the National Supercomputing Mission (NSM), Government of India.

References

- 1 S. Das, L. Acharya, L. Biswal and K. Parida, *Nanoscale Adv.*, 2024, **6**, 934–946.
- 2 U. Kumar and I. Sinha, *J. Environ. Chem. Eng.*, 2023, **11**, 111280.
- 3 J. Qiu, D. Dai and J. Yao, *Coord. Chem. Rev.*, 2024, **501**, 215597.
- 4 K. Mase, M. Yoneda, Y. Yamada and S. Fukuzumi, *ACS Energy Lett.*, 2016, **1**, 913–919.
- 5 L. Xie, X. Wang, Z. Zhang, Y. Ma, T. Du, R. Wang and J. Wang, *Small*, 2023, **19**, 1–25.
- 6 W. Yu, Z. Zhu, C. Hu, S. Lin, Y. Wang, C. Wang, N. Tian, Y. Zhang and H. Huang, *J. Mater. Chem. A*, 2023, **11**, 6384–6393.
- 7 X. Dang, S. Wu and H. Zhao, *ACS Sustainable Chem. Eng.*, 2022, **10**, 4161–4172.
- 8 L. Wang, J. Zhang, Y. Zhang, H. Yu, Y. Qu and J. Yu, *Small*, 2022, **18**, 2104561.
- 9 U. Kumar, A. Shrivastava and I. Sinha, *Catal. Sci. Technol.*, 2024, **14**(10), 2668–2883.
- 10 M. T. Ahmed, H. Abdullah and D. H. Kuo, *ACS Appl. Mater. Interfaces*, 2023, **15**, 29224–29235.
- 11 F. Wang, S. Yue, X. Han, T. Zhang, A. Han, L. Wang and J. Liu, *ACS Appl. Mater. Interfaces*, 2024, **16**, 2606–2613.
- 12 R. Li, D. Zhang, Y. Shi, C. Li, Y. Long and M. Yang, *J. Catal.*, 2022, **416**, 322–331.
- 13 U. Kumar, J. Kuntail, A. Kumar, R. Prakash, M. R. Pai and I. Sinha, *Appl. Surf. Sci.*, 2022, **589**, 153013.
- 14 M. A. Qaiser, S. Khan, W. A. Qureshi, S. N. uz Z. Haider, W. Wang and Q. Liu, *Int. J. Hydrogen Energy*, 2024, **95**, 935–956.
- 15 Y. He, Y. Wang, J. Qian, K. Xu, B. Lu, S. Tang, Y. Liu and J. Shen, *Appl. Catal., B*, 2025, **361**, 124565.
- 16 A. Shrivastava, U. Kumar and I. Sinha, *Ind. Eng. Chem. Res.*, 2024, **63**, 15721–15734.
- 17 Z. Zheng, F. Han, B. Xing, X. Han and B. Li, *J. Colloid Interface Sci.*, 2022, **624**, 460–470.
- 18 S. Mirsadeghi, H. Zandavar, H. R. Rajabi, F. Sajadiazl, M. R. Ganjali and S. M. Pourmortazavi, *J. Mater. Res. Technol.*, 2021, **14**, 808–821.
- 19 S. Pal, S. Kumar, A. Verma, A. Kumar, T. Ludwig, M. Frank, S. Mathur, R. Prakash and I. Sinha, *Mater. Sci. Semicond. Process.*, 2020, **112**, 105024.
- 20 S. Srivastava, R. Awasthi, N. S. Gajbhiye, V. Agarwal, A. Singh, A. Yadav and R. K. Gupta, *J. Colloid Interface Sci.*, 2011, **359**, 104–111.
- 21 T. T. Dung, T. M. Danh, L. T. M. Hoa, D. M. Chien and N. H. Duc, *J. Exp. Nanosci.*, 2009, **4**, 259–267.
- 22 G. Zuo, S. Liu, L. Wang, H. Song, P. Zong, W. Hou, B. Li, Z. Guo, X. Meng, Y. Du, T. Wang and V. A. L. Roy, *Catal. Commun.*, 2019, **123**, 69–72.
- 23 F. Saman, H. Bahruji, A. H. Mahadi and C. H. S. Ling, *Fuel*, 2023, **349**, 128725.
- 24 S. M. Hosseini, M. Ghiaci, S. A. Kulinich, W. Wunderlich, H. Farrokhpour, M. Saraji and A. Shahvar, *J. Phys. Chem. C*, 2018, **122**, 27477–27485.
- 25 H. Song, L. Wei, C. Chen, C. Wen and F. Han, *J. Catal.*, 2019, **376**, 198–208.
- 26 D. Tsukamoto, A. Shiro, Y. Shiraishi, Y. Sugano, S. Ichikawa, S. Tanaka and T. Hirai, *ACS Catal.*, 2012, **2**, 599–603.
- 27 S. Ma, Y. Yang, J. Li, Y. Mei, Y. Zhu, J. Wu, L. Liu, T. Yao and Q. Yang, *J. Colloid Interface Sci.*, 2022, **606**, 1800–1810.
- 28 U. Kumar, A. Shrivastava, A. K. De, M. R. Pai and I. Sinha, *Catal. Sci. Technol.*, 2023, **13**(8), 2432–2446.
- 29 F. Sun, Q. Jing, T. Xing, Y. Li, B. Jiang, Y. Zhao and H. Wang, *ACS Sustainable Chem. Eng.*, 2025, **13**(12), 4873–4883.
- 30 U. Kumar, E. Picheau, H. Li, Z. Zhang, T. Kikuchi, I. Sinha and R. Ma, *ACS Appl. Energy Mater.*, 2025, **8**(5), 3107–3119.
- 31 W. Yu, Z. Zhu, C. Hu, S. Lin, Y. Wang, C. Wang, N. Tian, Y. Zhang and H. Huang, *J. Mater. Chem. A*, 2023, **11**, 6384–6393.
- 32 A. Shrivastava, J. Kuntail, U. Kumar and I. Sinha, *J. Mol. Liq.*, 2023, **389**, 122932.
- 33 X. Zhou, J. Liang, L. Xu, S. Wu, M. Xie, Q. Liang, J. Luo, X. Fan, X. Zhou and X. Zhou, *J. Colloid Interface Sci.*, 2025, **689**, 1–10.
- 34 Y. Xian, Z. Li, L. Peng, J. Luo, X. Ning, X. Zhou and X. Zhou, *Sep. Purif. Technol.*, 2024, **345**, 127337.
- 35 B. Sun, X. Sun, W. Chen, Y. Zhou, W. Zhang, Q. Nie, X. Lin, Y. Li and Y. Liu, *Colloids Surf., A*, 2025, **711**, 136384.
- 36 S. Pal, P. N. Singh, A. Verma, A. Kumar, D. Tiwary, R. Prakash and I. Sinha, *Environ. Nanotechnol., Monit. Manage.*, 2020, **14**, 100311.
- 37 A. Bumajdad, S. Ali and A. Mathew, *J. Colloid Interface Sci.*, 2011, **355**, 282–292.



- 38 W. Huang, C. Jing, X. Zhang, M. Tang, L. Tang, M. Wu and N. Liu, *Chem. Eng. J.*, 2018, **349**, 603–612.
- 39 Y. Ma, M. Fa, Y. Zhang, L. Xiong, X. Li and S. Zhou, *Int. J. Hydrogen Energy*, 2025, **116**, 378–388.
- 40 S. Li, G. Dong, R. Hailili, L. Yang, Y. Li, F. Wang, Y. Zeng and C. Wang, *Appl. Catal., B*, 2016, **190**, 26–35.
- 41 Z. Lu, Z. Yu, J. Dong, M. Song, Y. Liu, X. Liu, Z. Ma, H. Su, Y. Yan and P. Huo, *Chem. Eng. J.*, 2018, **337**, 228–241.
- 42 X. An, K. Li and J. Tang, *ChemSusChem*, 2014, **7**, 1086–1093.
- 43 W. Zhang, C. Jiang, H. Guan, Y. Wang, Y. Hu, W. Wang, W. Tian and L. Hao, *Mater. Adv.*, 2024, **5**, 1340–1347.
- 44 M. Hua, L. Xu, F. Cui, J. Lian, Y. Huang, J. Bao, J. Qiu, Y. Xu, H. Xu, Y. Zhao and H. Li, *J. Mater. Sci.*, 2018, **53**, 7621–7636.
- 45 N. A. Zubir, C. Yacou, J. Motuzas, X. Zhang and J. C. Diniz Da Costa, *Sci. Rep.*, 2014, **4**, 1–8.
- 46 N. Padmavathy, I. Chakraborty, A. Kumar, A. Roy, S. Bose and K. Chatterjee, *ACS Appl. Nano Mater.*, 2022, **5**, 237–248.
- 47 J. Cheng, Z. Niu, Z. Zhao, X. Pei, S. Zhang, H. Wang, D. Li and Z. Guo, *Adv. Energy Mater.*, 2023, **13**(5), 2203248.
- 48 T. L. Xi, L. J. Liu, Q. Liu, H. W. Wang, L. Y. Zuo, H. T. Fan, B. Li and L. Y. Wang, *Int. J. Hydrogen Energy*, 2024, **62**, 62–70.
- 49 T. Garg, Nitansh, S. Kaur, P. Kaur, B. Singh and S. Singhal, *Appl. Mater. Today*, 2025, **43**, 102650.
- 50 C. Singh, Devika, R. Malik, V. Kumar and S. Singhal, *RSC Adv.*, 2015, **5**, 89327–89337.
- 51 D. Sebastia-Saez, S. Gu and M. Ramaioli, *Chem. Eng. Sci.*, 2018, **176**, 356–366.

